PHYSICS

Van der Waals mid-wavelength infrared detector linear array for room temperature passive imaging

Tengfei Xu[1,2]†, Fang Zhong[3]†, Peng Wang[2,4]*, Zhen Wang[2], Xun Ge[2], Jinjin Wang[2,4], Hailu Wang[2], Kun Zhang[2], Zhenhan Zhang[2,5], Tiange Zhao[2], Yiye Yu[2,6], Min Luo[2,4], Yang Wang[2,5], Ruiqi Jiang[2], Fang Wang[2], Fansheng Chen[2], Qi Liu[1], Weida Hu[2,4]*

Passive imaging for mid-wave infrared (MWIR) is resistant to atmospheric pollutants, guaranteeing image clarity and accuracy. Arrayed photodetectors can simultaneously perform radiation sensing to improve efficiency. Room temperature van der Waals (vdWs) photodetectors without lattice matching have evolved rapidly with optimized stacking methods, primarily for single-pixel devices. The urgent need to implement arrayed devices aligns with practical demands. Here, we present an 8 by 1 black phosphorus/molybdenum sulfide (BP/MoS_2) vdWs photodetector linear array with a fill-factor of ~77%, fabricated using a temperature-assisted sloping transfer method. The flat interface and uniform thickness facilitate carrier transport and minimize pixel nonuniformities, showing an average peak detectivity (D^*) of 2.34 × 10^9 cm·$Hz^{1/2}$·W^{-1} in the mid-wave infrared region. Compared to a single pixel, push-broom scanning passive imaging is eight times more efficient and further enhanced through mean filtering and fast Fourier transform filtering for strip noise correction. Our study offers guidance on vdWs arrayed devices for engineering applications.

INTRODUCTION

Mid-wave infrared (MWIR) in the range of 3 to 5 μm is one of the primary atmospheric windows for infrared radiation, with atmospheric transmittance reaching as high as 80 to 85%. Passive imaging technology for MWIR can effectively penetrate common atmospheric pollutants, enabling the better capture of thermal radiation signals from target objects and providing improved imaging results even in complex environmental conditions. This technology plays an important role in various fields such as security, medical, and industrial applications (*1*–*3*). Infrared (IR) photodetectors are the core components of passive imaging technology to sense and receive IR radiation signals. These photodetectors are generally based on narrow bandgap semiconductor materials or special structures, such as InSb (*4*), HgCdTe (*5*), and type II superlattice (*6*). After decades of development, these detectors have been scaled up to focal plane arrays (*7*). However, the epitaxial growth process of these materials is still susceptible to lattice mismatch and involves toxic materials. Moreover, such detectors usually require a cooling system to reduce thermal noise and increase sensitivity in practical applications, which increases the complexity and cost of the imaging system.

Two-dimensional (2D) materials have shown great potential in photodetection. MoS_2, a key transition metal dichalcogenide (TMDC), is notable for its semiconductor traits, high carrier mobility, and chemical stability, making it ideal for optoelectronic devices, such as broadband photodetector and ultrafast photodiode (*8*, *9*). The stacking property enables advanced junction structures (*10*–*12*). In particular, the heterojunction constructed from atomically thin MoS_2 and carbon nanotubes demonstrates unprecedented gate tunability in both electrical and optical properties, which is not observed in bulk semiconductor devices (*13*). The trend of arrayed detectors has emerged and continues to expand in scale (*14*–*16*), but it remains limited to the visible spectrum due to wide bandgaps. Arrayed noble metal dichalcogenides with narrow bandgaps can be obtained by direct selenization (*17*) and tellurium-vapor transformation (*18*) methods. However, the materials obtained by such methods are generally polycrystalline along with abundant defects, which affects the performance and uniformity. In addition, dispersed pixels reduce the utilization efficiency of radiation incident on the pixels, and the extremely low fill-factor further limits the sensitivity of arrayed devices. Consequently, such detectors are often limited to applications in laser-assisted mask imaging, with a very restricted range of use cases. Black phosphorus (BP) is favored for MWIR optoelectronic applications due to its high mobility (*19*), tunable bandgap (*20*), and polarization sensitive (*21*). High-sensitivity photodiodes with polarization-sensitive detection capabilities have been successively reported (*22*, *23*), leading to functional devices such as image sensors (*24*), gas detectors (*25*), and spectrometers (*26*). BP-based photodetectors offer capabilities akin to camera detection chips (*27*, *28*), allowing for passive imaging at room temperature. However, the reported high-sensitivity photodetection is still limited to single-pixel photodetector, which can only collect imaging data pixel by pixel during passive imaging, making it much more challenging to obtain high-resolution images. The imminent need to unlock applications for arrayed BP-based devices is pressing, as the potential for broader, innovative uses becomes increasingly evident.

In this work, we report an 8 by 1 BP/MoS_2 van der Waals (vdWs) photodetector linear array fabricated by a temperature-assisted sloping transfer method. The arrayed photodetector with a high fill-factor exhibits an average peak detectivity (D^*) of 2.34 × 10^9 cm·$Hz^{1/2}$·W^{-1} at 3.6 μm at room temperature. The smooth interfaces and uniform thickness between pixels have been validated, providing a reliable basis for the excellent uniformity of optoelectronic performance among array pixels. The push-broom scanning system is used to verify the

[1]State Key Laboratory of Integrated Chips and Systems, Frontier Institute of Chip and System, Fudan University, Shanghai, China. [2]State Key Laboratory of Infrared Physics, Shanghai Institute of Technical Physics, Chinese Academy of Sciences, Shanghai, China. [3]Hangzhou Institute for Advanced Study, University of Chinese Academy of Sciences, Hangzhou, China. [4]University of Chinese Academy of Sciences, Beijing, China. [5]State Key Laboratory of ASIC and System, School of Microelectronics, Fudan University, Shanghai, China. [6]Wuhan National Laboratory for Optoelectronics, Huazhong University of Science and Technology, Wuhan, China.
*Corresponding author. Email: w_peng@mail.sitp.ac.cn (P.W.); wdhu@mail.sitp.ac.cn (W.H.)
†These authors contributed equally to this work.

passive imaging function of the linear array, and the eight-channel parallel readout method increases the efficiency by eight times compared to a single pixel, revealing the notable separation between targets and background under weak signal conditions. The appropriate nonuniformity denoising methods have proven highly beneficial in improving image quality and enhancing target recognition capability.

RESULTS

Device fabrication and characterizations

High-quality interface contact of all pixels in the array must be considered and solved when constructing a vdWs photodetector linear array. In our work, the narrow-bandgap BP flake is used as the p-type absorption layer, combined with the n-type MoS_2 to construct a photodiode. As shown in Fig. 1A, the ideal vdWs heterostructure generally manifests as atomically sharp interfaces, and photogenerated electron-hole pairs are effectively collected by the electrodes on both sides driven by the built-in electric field. Classic transfer methods for vdWs heterostructure using various media have provided numerous opportunities for constructing complex structures or functional semiconductor devices (*29*–*34*), which are typically categorized into wet transfer and dry transfer methods. On the basis of an in-depth study of the transfer process and interface issues, continually improved transfer methods have now enabled the creation of near-ideal, bubble-free heterostructures, which is crucial for developing devices based on high-quality vdWs heterostructures (*35*, *36*). Recent reports indicate that using transfer techniques to manufacture high-quality bubble-free vdWs heterostructure of arrays is not only entirely feasible but also highly promising. Research on interface engineering is crucial for achieving heterojunctions with highly uniform electrical conduction interfaces (*37*). As the scale increases, the transfer stacking of ideal interfaces faces substantial problems (Fig. 1, B and C). Specifically, the transition of 2D materials from a flexible polymer medium to a rigid substrate easily leads to stress release, causing material wrinkling (Fig. 1C, i). There is no effective contact between the two materials in these regions, and the misestimation of the effective area directly leads to an incorrect calculation of various figures of merit (*38*). On the other hand, the electron scattering caused by the flexural phonons generated by the wrinkled structure significantly reduces mobility (*39*). Even in cases of effective contact, rough interfaces often raise concerns (Fig. 1C, ii). Impurities or defects at the interfaces may act as trap centers, prolonging the carrier lifetime and sacrificing response time (*40*). Furthermore, the substrate is partially etched, roughened, and contaminated with adsorbates (*41*) when MoS_2 is etched into regular patterns (Fig. 1C, iii). Although surface unevenness may not substantially impede the stacking process, weak adhesion is highly prone to result in the subsequent detachment and displacement of heterojunctions, leading to irreversible damage to the arrayed devices.

To mitigate these adverse effects, we used a temperature-assisted sloping transfer method for the transfer of large-scale 2D materials, which was used in the fabrication of photodetector arrays (as shown in Fig. 1D and fig. S1). On one hand, the differences in the thermal expansion coefficients between polymers and inorganic materials are notable, allowing for an automated stacking process through the gradual expansion of the polymer during heating (*42*). On the other hand, a high temperature, contact angle between films, and slow contact speed are key factors in achieving high-quality bubble-free interfaces, providing valuable insights into interface engineering (*36*, *37*). The sloping angle guides the slow release and stacking of the heterostructure, as well as the release of interface contaminants, which is beneficial for the uniformity and contact quality of heterojunctions. The detailed process is described in the note S1. We used density functional theory (DFT) calculations to analyze the variation in adhesion energy during the transfer process. As shown in Fig. 1E, the adhesion energy between the polymer and BP gradually decreases during the thermal expansion process (from −0.4138 to −0.3904 eV), leading to a larger difference compared to the adhesion energy between BP and MoS_2 (−0.7909 eV). This implies a more favorable release of materials and interface bonding. The change in adhesion energy may be associated with the material lattice structure caused by thermal expansion, and the change in distance between atoms or molecules leads to a decrease in adhesion energy. The calculation details and structure are provided in note S2 and fig. S2. The specific transfer process is illustrated in Fig. 1D (i to iv). First, the BP was adjusted to ensure priority contact with specific edge of MoS_2 (Fig. 1D, i and ii). Second, polydimethylsiloxane gradually expands during the heating process to 35°C (typically 10°C higher than room temperature), and the contact interface was gradually released from one side to the other to minimize the presence of bubbles and wrinkles within the interface during the heating process (Fig. 1D, ii and iii). Then, polymethyl methacrylate was used as the mask for reactive ion etching to obtain the linear array device (Fig. 1D, iv).

As shown in Fig. 1F, cross-sectional transmission electron microscopy (TEM) measurements were performed on the BP/MoS_2 heterostructure to further validate the quality of the interface. The thicknesses of monolayer BP and MoS_2 are 6 and 5.5 Å, respectively. The TEM image reveals a vdWs interface with atomic-level flat contact, indicating the absence of lattice mismatch. The energy dispersive spectrometer mapping shows that no oxidation occurred between the BP and MoS_2 flakes during the entire transfer process, which was conducted in an N_2 protective atmosphere. This high-quality interface contact ensures efficient photoelectric conversion and charge transfer, laying the foundation for high-performance photodetection of the linear array device. The optical microscope photograph of the 8 by 1 BP/MoS_2 vdWs photodetector linear array is displayed in Fig. 1G, and BP and MoS_2 are marked in purple and blue regions, respectively. For arrayed IR detectors, pixels are divided into photosensitive and nonsensitive areas. The fill-factor is defined as the ratio of the pixel's photosensitive area to the product of the lateral and vertical center-to-center distances between adjacent pixels, which has been widely adopted in the context of arrayed devices (*43*). The calculation method is shown in fig. S3. In our work, the fill-factor is approximately 77%. The height result of the linear array extracted by atomic force microscopy (AFM) is shown in Fig. 1H, which indicates a thickness of approximately 92 nm for a heterostructure (indicated by the red line in Fig. 1G). Meanwhile, the method of reactive ion etching can effectively separate different pixels, and the gap between the two pixels is very obvious (Fig. 1I, indicated by the blue line in Fig. 1G). The thickness of all pixels is summarized in Fig. 1J, and detailed thickness information is displayed in fig. S4. Since all pixels of linear array device come from the same material, the thickness of all pixels remains around 90 nm, which can reduce device deviations caused by thickness differences, ensuring that these pixels have similar photoelectric characteristics during the photoelectric conversion process, thereby achieving closer signal detection capabilities.

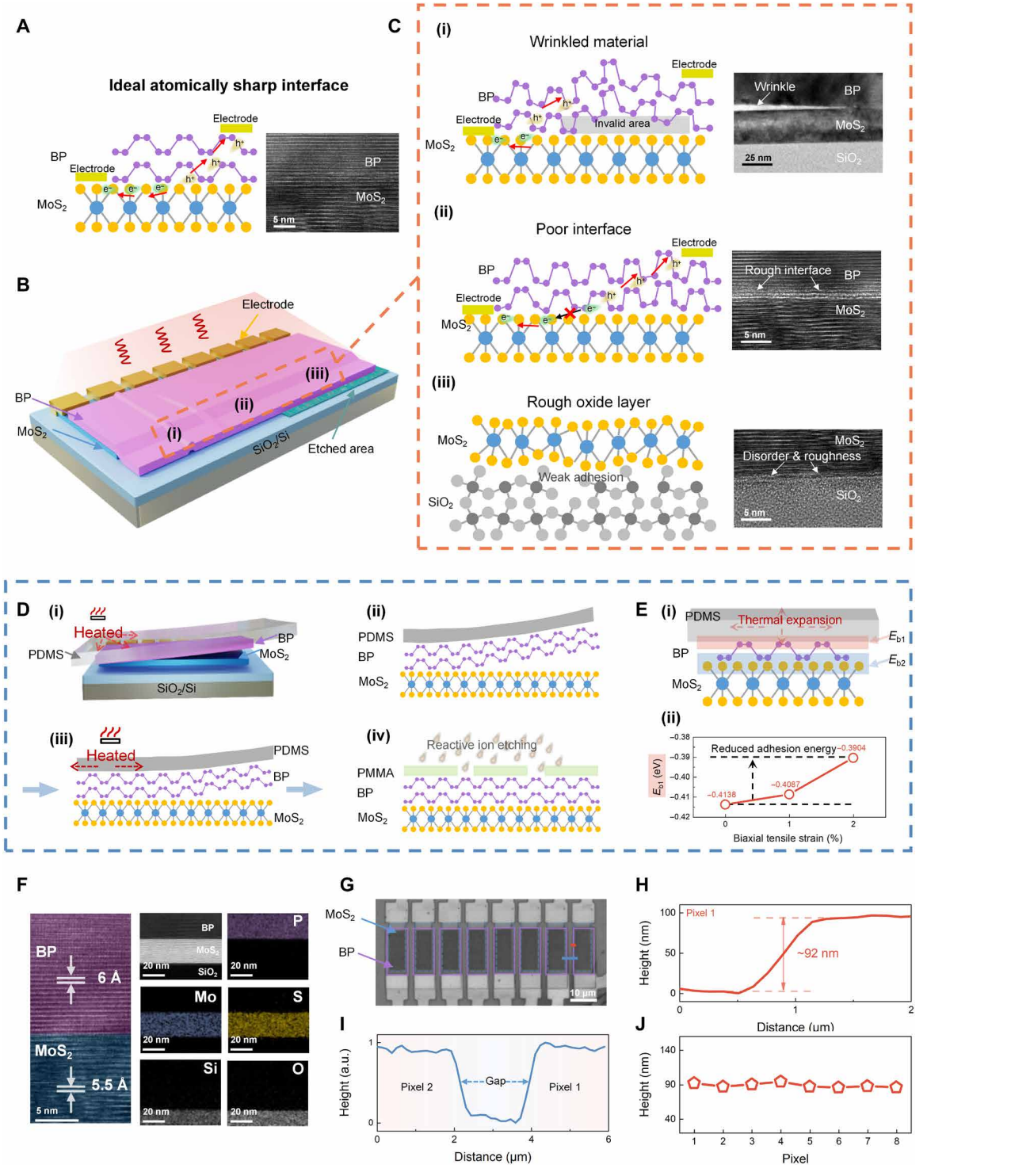

Fig. 1. Schematic diagram of the fabrication and characterizations for vdWs photodetector linear array. (**A**) Ideal BP/MoS_2 vdWs heterostructure contact with sharp and clear interface. Left: Schematic diagram of molecular structure and transport of photogenerated carriers. Right: Cross-sectional TEM image of the ideal interface. (**B** and **C**) Problems in the stacking of large-scale 2D materials, including wrinkled material (i), poor interface (ii), and weak adhesion (iii). Cross-sectional TEM images were captured under these phenomena. (**D**) Fabrication process for vdWs photodetector linear array. Schematic diagram of temperature-assisted sloping transfer method (i); adjust the tilt angle of BP to contact with the edge of MoS_2 (ii); contact interface was released during the heating process (iii); polymethyl methacrylate (PMMA) as a mask for reactive ion etching(iv). (**E**) Schematic diagram of adhesion energy for polydimethylsiloxane (PDMS)/BP (E_{b1}) and BP/MoS_2 (E_{b2}) (i) calculated by DFT, showing reduced adhesion energy E_{b1} (ii). (**F**) Cross-sectional TEM image and energy dispersive spectrometer mapping of BP/MoS_2 vdWs heterojunction, showing the unoxidized atomically flat contact. (**G**) Optical microscope photograph of the 8 by 1 BP/MoS_2 vdWs photodetector linear array. (**H** to **J**) Thickness measurement of linear array, including the heterostructure (H), normalized gap (I) and statistics of all the pixels (J). a.u., arbitrary units.

Optoelectronic properties of BP/MoS_2 vdWs photodetector linear array

With high-quality interface contact and well thickness uniformity as prerequisites, the optoelectronic properties of the BP/MoS_2 vdWs photodetector linear array were further characterized at room temperature under zero bias. Figure 2 (A and B) shows a schematic diagram of a linear array and a detailed structural diagram of the pixel, respectively. In our study, we implemented a heterojunction configuration of p-type BP stacked on n-type MoS_2. Photodiodes with similar structures have been shown to exhibit excellent performance for IR photodetection (*22*, *27*, *28*). Figure 2C displays the *I-V* curve of the linear array, consistently exhibiting the typical rectification behavior of the pn junction. Still noticeable are the differences in the *I-V* curves among different pixels, likely attributable to the uneven distribution of carrier concentration caused by subtle differences in thickness (*44*). Significant band bending occurs under large reverse bias voltages, increasing the probability of tunneling and amplifying differences in electrical performance. Furthermore, polymer contamination during device fabrication, inherent nonuniformity of the dielectric, and localized charge impurities evolving during measurements can also adversely affect the electrical performance of array devices (*45*, *46*). We provide a detailed analysis of the dark current in note S3. In addition, arrayed devices can also be fabricated by previously reported transfer methods (*31*, *32*). However, nonuniform contact and residual polymers significantly affect the uniformity of device performance. We conducted a detailed comparative analysis of the *I-V* curves of arrayed devices fabricated by different methods, as described in figs. S5 and S6 and notes S4 and S5. Compared to other methods, our approach benefits from improved processes, resulting in uniform contact interfaces, presenting more similar *I-V* curves between pixels with differences less than an order of magnitude. To determine the spectral response range, we performed a spectral response measurement by a Fourier transform infrared spectrometer on the BP/MoS_2 IR photodetector. As shown in Fig. 2D, our device exhibits peak response and cutoff wavelengths of approximately 3.6 and 3.8 μm, respectively, indicating the detection capabilities in the MWIR at room temperature. Furthermore, we use a wavelength-tunable MWIR pulse laser to characterize the mid-IR detection performance of the device. As displayed in Fig. 2E, time response curves are obtained at wavelengths of 2.6, 3.1, 3.4, 3.6, 3.8, 4.0, 4.1, and 4.2 μm. Stable performance at different wavelengths demonstrates the reliability of photoresponse in vdWs photodetector linear array.

To clarify the photoresponse mechanism of the BP/MoS_2 photodetector under the zero bias operating mode, we prepared a single-pixel vdWs photodiode with sharp edges and measured their photocurrent generation positions using scanning photocurrent microscope mapping measurement under 637 nm and 2-μm laser illumination, as shown in fig. S7. It can be observed that the photoresponse originates from the junction region and exhibits consistent sharp edges, indicating that an effective junction can drive the separation of photo-generated carriers. Response time is an important parameter to assess a photodetector's response capability. In this work, we used two methods to extract the response time of the photodetector. The corresponding frequency when the photoresponse decreases to an initial 0.707 times is defined as the cutoff frequency *f*, also known as −3-dB bandwidth (*38*). As shown in Fig. 2F, the cutoff frequency of the detector was obtained at 4 kHz using a blackbody as the radiation source. The τ_{rising} can be calculated to be approximately 87.5 μs using the formula $\tau_{rising} = 0.35/f(-3\ \mathrm{dB})$. On the other hand, the response time of the photodetectors is extracted from the time-resolved response measured by a commercial oscilloscope with a 2-μm laser illumination. As shown in Fig. 2G (up), τ_{rising} and $\tau_{falling}$ are 56 and 79 μs, respectively. The slight differences in response time obtained from different methods are mainly related to the incident light source. Compared to a laser, the blackbody radiation source covers the entire spectrum, making it difficult to focus. However, both methods yield results that reflect the detector's ability to respond quickly to signals (*27*). As shown in Fig. 2G (down) and fig. S8, the rising time and falling time of the linear array device exhibit excellent uniformity, indicating that each pixel can rapidly respond when the light signal arrives and quickly recover to its normal state when the light signal disappears. This consistent and fast response capability is crucial for a photodetector linear array, as it ensures accurate capture of signals and reduces errors and uncertainties caused by variations in response times between pixels. The relationship between photocurrent and incident intensity can be expressed as $I_{ph} = cP^{\alpha}$, where *c* is a constant and *P* is the incident light power, and α is obtained from the power law relationship. Figure 2H (up) shows the measured and fitted variation of photocurrent with incident intensity, resulting in a nonlinear fitting value of $\alpha = 0.95$. Excellent linearity can be well maintained under laser irradiation at other wavelengths as well (Fig. 2H, down, and fig. S9), indicating that the photocurrent steadily increases linearly with the incident power whether at longer or shorter wavelengths. Internal quantum efficiency (*IQE*) is the ratio of collected charge carriers (N_C) to the number of photons absorbed by the device (N_A), which can be expressed as $IQE = N_C/N_A = Rhc/\eta e\lambda$, where *R* is the responsivity, *h* is the Planck constant, *c* is the speed of light, η is the light absorption efficiency, *e* is the electron charge, and λ is the wavelength of the incidence light. As shown in fig. S10, The *IQE* of all pixels remains around 20%, consistent with previous discussions. Figure 2I and fig. S11 display the spectral noise current of the detector linear array. The noise currents are close to the testing limits of the system, and all pixels exhibit noise currents within the same order of magnitude, showing great uniformity. The consistent noise characteristics among different pixels ensure the steadiness of the detector linear array during operation.

Specific detectivity (D^*) is another important performance parameter of IR photodetectors. We investigate the photoelectric characteristics of photodetector linear array under blackbody radiation at room temperature. Here, D^* can be calculated by the equation: $D^* = (A\Delta f)^{1/2}/NEP = R(A\Delta f)^{1/2}/i_N$, where i_N is the noise current, *R* is the responsivity, *A* is the effective area of the photodetector, and Δf is the bandwidth (*38*). The room temperature D^* as a function of wavelength for one pixel of the linear array at different blackbody temperatures is shown in Fig. 3A. Room temperature peak D^* is up to 2.58×10^9 cm·$Hz^{1/2}$·W^{-1} in the MWIR region, and it always remains constant as the blackbody temperature changes. As shown in Fig. 3B, similar phenomena can be observed in the other pixels of the photodetector linear array, and room temperature peak D^* at different blackbody temperatures was calculated to demonstrate the stability of the detector linear array. The improved fabricating process takes into account both the performance of a single pixel and the overall uniformity of the array. For one pixel, peak D^* remains relatively constant with varying blackbody

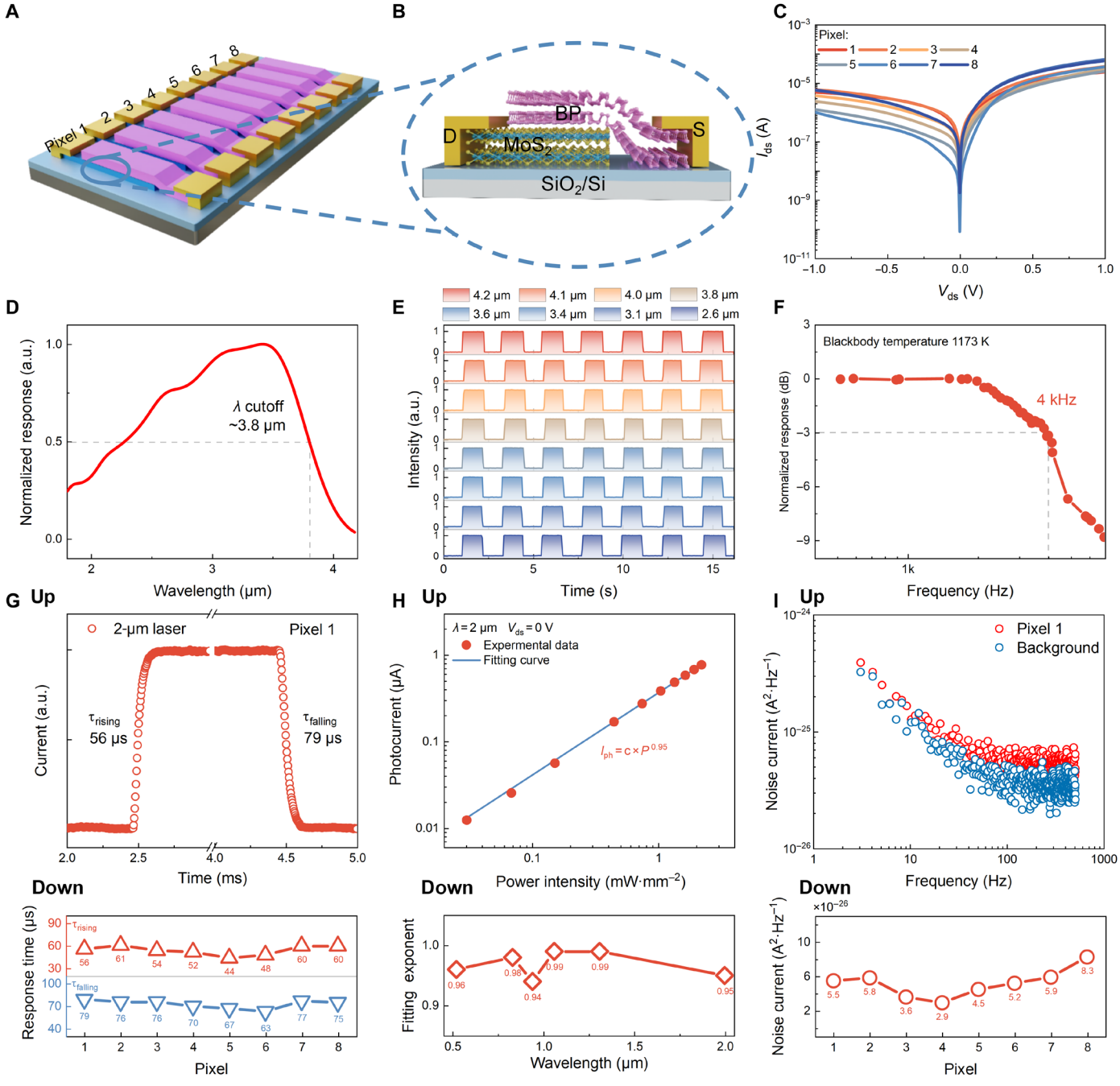

Fig. 2. Optoelectronic characteristics of vdWs photodetector linear array at room temperature. (**A** and **B**) Schematic diagram of the BP/MoS_2 vdWs photodetector linear array (A) and detailed structural diagram of a heterojunction (B). (**C**) *I-V* characteristic curves of all pixels in linear array. (**D**) Normalized spectral response of the BP/MoS_2 photodetector with a cutoff wavelength at approximately 3.8 μm. (**E**) Time response curves are obtained under a modulated MWIR illumination source, showing stable photoresponses during photodetection. (**F**) Relative response versus switching frequency with 1173 K blackbody temperature as the source, indicating a −3-dB cutoff frequency of 4 kHz. (**G**) Response time of a BP/MoS_2 device (up) and the statistics of all the responsive pixels (down) with 2-μm laser as the source. (**H**) Power dependence of a BP/MoS_2 device (up) under 2-μm laser illumination and the statistics of fitting factors under laser illumination of other wavelengths (down). (**I**) Spectral noise current of a BP/MoS_2 device (up) along with the background and the statistics of all the responsive pixels (down).

temperatures, exhibiting stable room temperature IR detection ability. For different pixels, in Fig. 3C, the peak D^* remains at the same magnitude of 10^9 even at different blackbody temperatures, which means that photodetector linear array can provide stable and similar signals at the same radiation. Here, the average blackbody peak D^* reaches 2.34×10^9 cm·$Hz^{1/2}$·W^{-1}, providing the opportunity to use other means to mitigate the impact of performance nonuniformity. The $D^*(\lambda)$ of the BP/MoS_2 vdWs photodetector linear array is compared with other commercial noncooled IR photodetectors in Fig. 3D, demonstrating performance on par with commercial

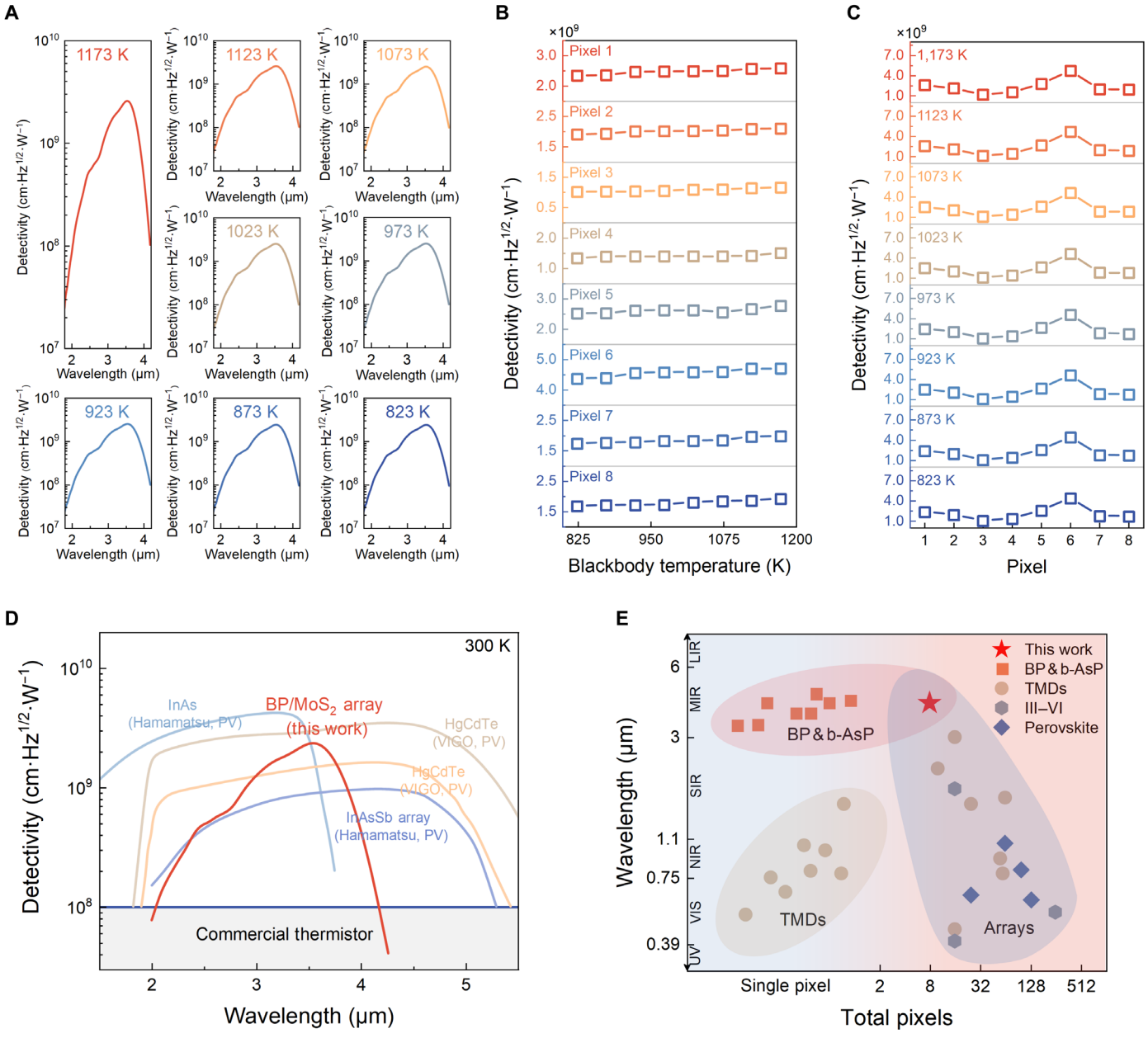

Fig. 3. Optoelectronic characteristics of vdWs photodetector linear array with blackbody as the source at room temperature. (**A**) D^* of one pixel as a function of wavelength at different blackbody temperatures. (**B** and **C**) Peak D^* of a pixel (B) and the photodetector linear array (C) at different blackbody temperatures demonstrate the stability of the photodetector linear array. (**D**) Blackbody detectivity comparison of 8 by 1 BP/MoS_2 vdWs photodetector linear array with other commercial room temperature IR photodetectors, including InAs (Hamamatsu, P10090-01), InAsSb array (Hamamatsu, P15742-016DS), HgCdTe (VIGO, PV-5-AF1 × 1-TO39-NW-90), and HgCdTe (VIGO, PV-5-AF0.1 × 0.1-TO39-NW-90) photodetectors. PV, photovoltaic. (**E**) Wavelength coverage range and pixel scale of 2D material photodetectors. UV, ultraviolet; VIS, visible; NIR, near infrared (0.75 to 1.1 μm); SIR, short-wave infrared (1 to 3 μm); MIR, mid-wave infrared (3 to 5 μm); LIR, long-wave infrared (8 to 12 μm).

devices and showcasing the potential of our arrayed detector in room temperature IR photodetection. Figure 3E shows a comparison of the scale and detection wavelength range of representative 2D material–based single-pixel and arrayed photodetectors at room temperature. Our work successfully extends the photodetection capability of BP-based photodetectors to linear arrays and achieves photodetection in the MWIR range compared to other 2D material arrayed photodetectors.

Room temperature push-broom scanning passive imaging and image nonuniformity correction

The eight-channel passive imaging system was designed to verify the passive detection capability of vdWs photodetector linear array. The schematic diagram of the passive imaging system was presented in Fig. 4A, where the linear array was used in place of the camera's detection chip, and a glass-sealed U-shaped curved carbon fiber heating tube was used as a blackbody-like radiation heat source. As the

pixels are not identical, the data were preprocessed on the basis of the set normalization parameters, mainly including the dark current and photocurrent, which is a common practice in arrayed device imaging (*47*). As depicted in Fig. 4B, the dark current of the linear array devices is subtracted and zeroed to ensure that the net photocurrent is collected during imaging, and then the amplification factor of each pixel in the array is adjusted to make the response signal as consistent as possible when the light source is activated. After preprocessing the dark current and photocurrent of the photodetector linear array, we conducted push-broom scanning passive imaging at room temperature. As shown in Fig. 4C, the arrayed detector was driven to the desired *XY* positions by stepper electrodes. The target signal was captured by the imaging lens and received by the photodetector linear array, and imaging results were mapped in real time on a computer. With the high sensitivity of the linear array, the image displays the distinct curved and straight features of the U-shaped heating tube. Furthermore, the U-shaped target and the background environment are successfully differentiated, resulting in a clear contrast and providing a reliable foundation for accurate target identification and analysis in the imaging results. We provide a comparison of reported arrayed 2D material photodetectors and our work in table S1. The scale of current photodetector arrays is relatively large

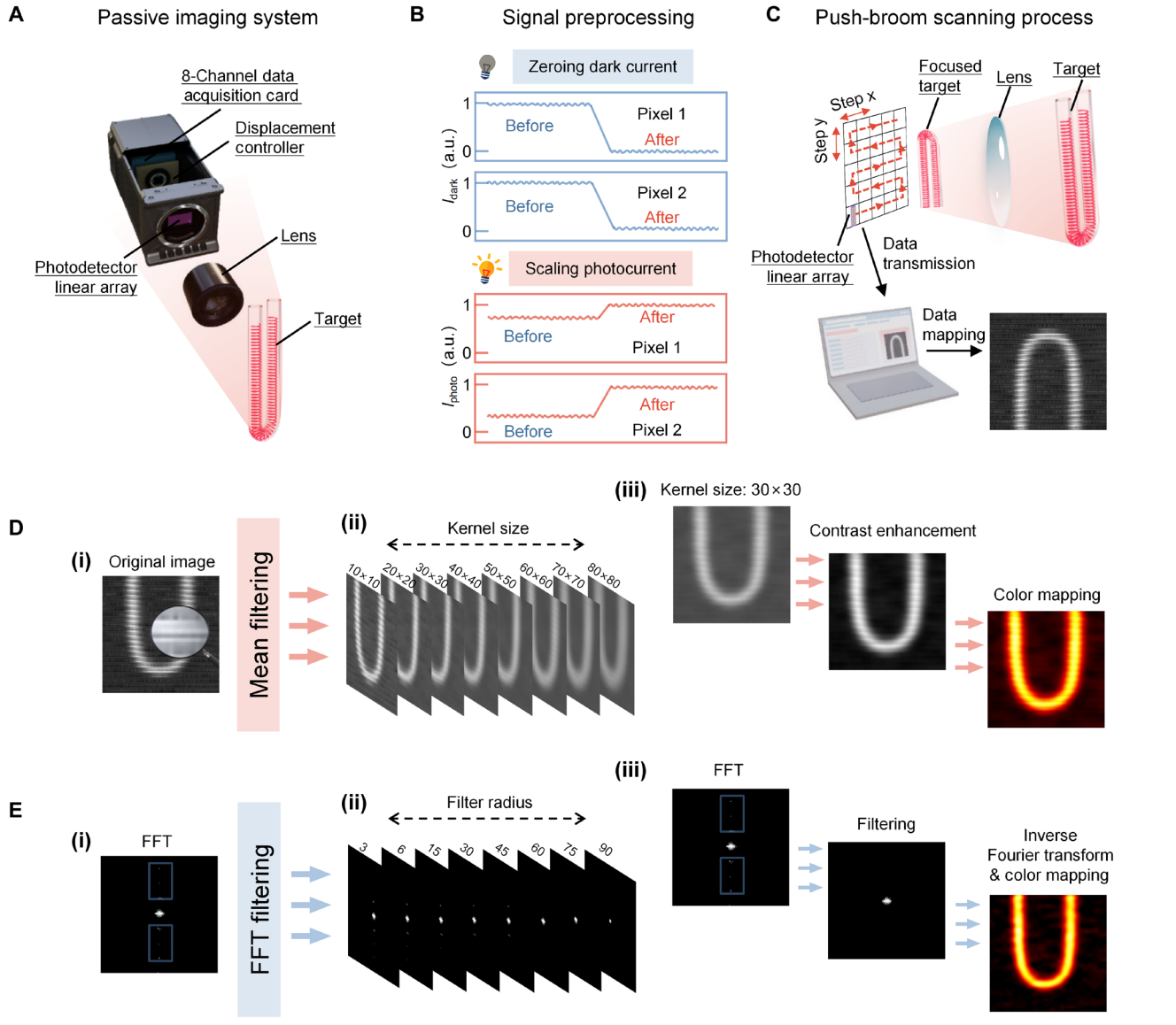

Fig. 4. Room temperature push-broom scanning passive of vdWs photodetector linear array and nonuniformity correction of the image. (**A**) Schematic diagram of the eight-channel passive imaging system, where the stepper motor drives the detector to the set *XY* position, and the photoresponse signal is collected by an eight-channel data acquisition card. (**B**) Schematic diagram of the signal preprocessing includes zeroing dark current and scaling photocurrent. (**C**) Schematic diagram of push-broom scanning process, results were mapped in real-time on a computer. (**D**) Process of nonuniformity correction of the image using mean filtering. Original image (i); filtered image with different kernel sizes (ii); contrast enhancement and color mapping after filtering (iii). (**E**) Process of nonuniformity correction of the image using FFT filtering. Frequency spectrum of the original image after FFT (i); filtered image with different filter radii (ii); inverse Fourier transform and color mapping after filtering (iii).

due to the large-area thin-film growth processes such as chemical vapor deposition (*48*, *49*), metal-organic chemical vapor deposition (*50*, *51*), molecular beam epitaxy (*47*, *52*), tellurization (*18*), and selenization (*53*). Many outstanding works have been reported, including 8 × 8 MoS_2 (*15*), 8 × 8 $MoSe_2$ (*48*), and 1 × 10 $PtSe_2$ (*53*). However, the photoelectric response of such photodetector arrays relies on the laser as the light source, which fails to achieve the response of blackbody radiation. Imaging capabilities have been widely proven in these arrayed devices, but imaging objects must be illuminated by external laser sources, and the imaging results only contain pattern information. We provide a detailed discussion of our work and representative TMDC-based arrayed devices in terms of wavelength range, blackbody response, imaging methods, and imaging results in note S6. In our work, we constructed a high fill-factor 8 by 1 MWIR photodetector linear array with blackbody response and used a push-broom scanning method to image objects in real scenes, displaying the shape characteristics and temperature distribution. The stable operational state and consistent performance of the BP/MoS_2 vdWs photodetector linear array are demonstrated. This achievement holds significant implications for the development of accurate and reliable high-performance photoelectric detection and passive imaging at room temperature.

The preprocessing technique of scaling the photocurrent of different pixels to the same level is only partially effective in reducing the variability among pixels. This residual nonuniformity leads to the presence of strip noise in the imaging results. Such noise is a common occurrence in linear array detectors, often manifesting as parallel stripes or noticeable color variations, impeding visual perception and information extraction. Two nonuniformity correction algorithms, mean filtering and fast Fourier transform (FFT) filtering, are used to alleviate strip noise and rectify the image. The detailed process is shown in note S7. Figure 4D and fig. S12 illustrate the process of applying mean filtering to the image. Mean filtering is the process of averaging the grayscale values of pixels within a rectangular area around each pixel and replacing the original pixel value with this average value (*54*, *55*). The size of the rectangular region is referred to as the kernel size, which determines the range and extent of the mean filtering. As shown in Fig. 4D (i), a notable reduction can be observed in stripe noise under an appropriate filter, and excessive or insufficient filtering leads to incomplete noise processing and image distortion (Fig. 4D, ii). The method of reallocating center pixel values may reduce the difference between surrounding pixels, manifested as a larger kernel leading to a decrease in image contrast. The contrast enhancement algorithm can improve the contrast of the image after mean filtering and reduce the blurring effect. In Fig. 4D (iii), contrast enhancement is applied to remap pixel values to a wider range, enhancing color contrast between the target and background, and improving clarity and visual effects. Last, the grayscale level of the image is mapped to a color space with flame colors to enhance expressiveness.

Unlike mean filtering, FFT filtering selectively removes or suppresses noise or interference by transforming the image from the spatial domain to the frequency domain (*56*, *57*). Figure 4E and fig. S13 show the process of FFT filtering to the image. Figure 4E (i) displays the frequency spectrum of the original image after FFT. The blue rectangular region highlights the frequency components associated with strip noise. It should be noted that the frequency spectrum is not a visualization of the image itself but represents the image in the frequency domain. After filtering the noise frequency components from the frequency spectrum using different radii, the essential frequency components of the original image are preserved (Fig. 4E, ii). Subsequently, the filtered frequency spectrum is inverse Fourier transformed to convert it back to the spatial domain, resulting in the image after FFT filtering. Figure 4E (iii) demonstrates the application of contrast enhancement and color mapping to the filtered image, further enhancing its quality and visual impact. The calibrated image exhibits improved contrast, brightness, and color representation. Both nonuniformity correction algorithms effectively mitigate strip noise and exhibit their characteristics. Mean filtering corrects nonuniformity by locally averaging in the image, while FFT filtering suppresses strip noise by eliminating noise-related components in the frequency domain. The calibrated images still preserve the original features of the targets, which holds great significance for subsequent image analysis, processing, and applications.

To assess the efficacy of nonuniformity correction for push-broom scanning imaging, we compared it with uniform single-pixel imaging. Mean squared error (MSE) and root mean squared error (RMSE) were used as metrics to quantify the similarity between two images, providing a more intuitive measure of their differences (*58*, *59*). Figure 5A illustrates the calculation process of MSE and RMSE. For MSE, the squared difference between the pixel values at each pixel position (i and j) in the two images is computed. The sum of all pixel positions is then divided by the total number of pixels to obtain the MSE. Taking the square root of MSE yields the RMSE. Hence, smaller values for MSE and RMSE indicate a higher degree of similarity between the two images. In Fig. 5 (B and C), the mean filtering method corresponds to MSE of 451.21 and RMSE of 21.24, while the FFT filtering method resulted in MSE of 203.71 and RMSE of 14.27. In addition, we considered a comparison of different filtering degrees on the impact of image denoising in Fig. 5 (D and E). A trade-off between noise reduction and the preservation of critical image features must be considered. Selecting an appropriately sized filter can effectively mitigate striping noise in the image, while excessive denoising can lead to image distortion. Overall, the nonuniformity correction process significantly addresses the challenges posed by the uneven response of array devices, achieving a similar level of quality and detail as single-pixel imaging.

DISCUSSION

In this study, we demonstrated a systematic investigation of an 8 by 1 vdWs BP/MoS_2 photodetector linear array with a fill-factor of ~77% for room temperature passive imaging. The confirmation of high uniformity in optoelectronic and spectral performance underscores the operability of the fabrication processes, showing an average blackbody peak room temperature D^* of 2.34×10^9 cm·$Hz^{1/2}$·W^{-1} near 3.6 μm under blackbody radiation. Push-broom scanning passive imaging was demonstrated using a multichannel parallel acquisition method, and nonuniformity correction algorithms were used to reduce the strip noise caused by nonuniform responses between pixels, approaching the ideal state of uniform imaging. Certainly, it cannot be denied that the scale we have achieved so far remains relatively limited due to the constraints imposed by large-area single-crystal thin-film materials. We believe that overcoming scalability limitations in the future primarily involves addressing growth and transfer of wafer-scale films, including materials like BP, Te, TMDCs, and other 2D materials. Mechanical exfoliation

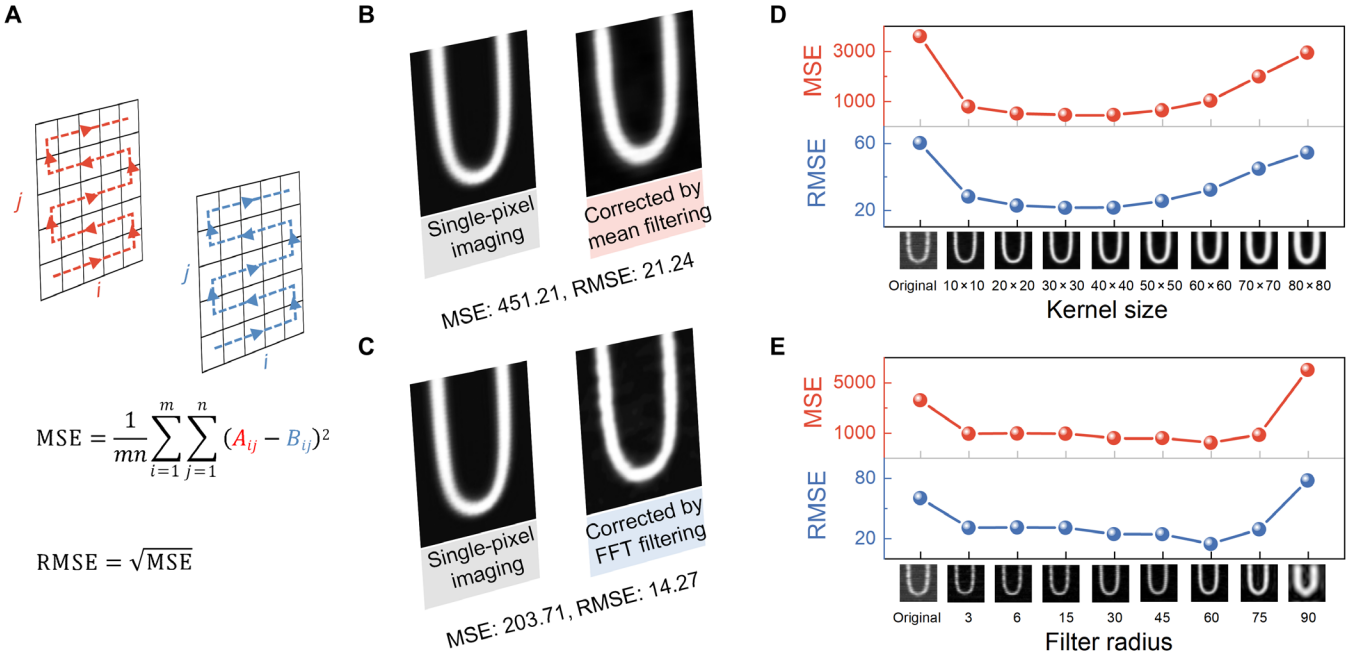

Fig. 5. Similarity evaluation of corrected image. (**A**) Calculation methods of the similarity metrics MSE and RMSE for images. (**B** and **C**) Similarity between the uniform single-pixel imaging and the corrected push-broom scanning imaging by mean filtering (B) and FFT filtering (C). (**D** and **E**) Similarity of images processed by mean filtering (D) and FFT filtering (E) with different sizes and radii indicates the importance of the appropriate degree of filtering.

remains a practical method for obtaining high-quality single-crystal films from bulk materials in the short term. Further development is needed for the large-area exfoliation and transfer methods. This not only involves stability and quality control of the material itself but also addresses several technical challenges during integration, such as optimizing interface, reducing polymer residue, avoiding contamination from organic solvents, and controlling the release of stress. Another approach to overcoming scalability limitations will primarily involve resolving the challenges associated with the growth of wafer-scale single-crystal films. Although the current BP films are still polycrystalline, with small grain boundaries and large polycrystalline cells, they show great potential for gradually achieving development (*60*, *61*). The instability of BP related to oxygen, water, and light remains an important issue that needs to be addressed. Although methods such as physical encapsulation and surface modification have been developed to temporarily improve stability, further research into the oxidation mechanisms of BP is still required to develop more reliable and lasting stability solutions (*62*). Concurrently, developing alternative material systems has become an indispensable direction for progress. Te can maintain a relatively stable state in the air without oxidation (*63*). Photodetectors based on Te have demonstrated excellent sensitivity in the IR range, making it a candidate material for MWIR detection (*64*). We believe that focal plane array devices will demonstrate significant potential for widespread adoption and application in various scenarios in the near future, with breakthroughs in thin-film epitaxial growth technology. We have provided a more detailed discussion in note S8. Our work represents a meaningful exploration of the current design and fabrication of vdWs arrayed devices, offering a new direction and reference for low-dimensional MWIR arrayed photodetectors in engineering applications.

MATERIALS AND METHODS

Device fabrication characterizations and measurements

Thin layers of BP and MoS_2 were obtained by mechanical exfoliation inside a glove box under a nitrogen atmosphere. The two materials were then dry-transferred and stacked to form a vdWs heterostructure. Electron beam lithography was used to pattern the electrodes, followed by the deposition of metal electrodes (Cr/Au with thicknesses of 15/75 nm) using vacuum thermal evaporation. After the electrode fabrication, mask windows were defined by electron beam lithography, followed by reactive ion etching to remove the corresponding areas of the materials to form the heterostructure linear array. More detailed processes can be found in note S1.

Characterizations and measurements

The interface of the heterostructure was measured using TEM (JEOL JEM-2100F). The height distribution of the heterostructure was obtained using a commercial AFM instrument (Oxford, MFP-3D). Electrical and optoelectronic measurements were conducted under ambient atmospheric conditions using confocal microscopy and an Agilent 2902 semiconductor parameter analyzer. A broadly tunable continuous MWIR laser was provided by a plasma laser. The MWIR laser response of the photodetector was tested using a wavelength-tunable mid-IR plasma laser (2.6, 3.1, 3.4, 3.6, 3.8, 4.0, 4.1, and 4.2 μm). The relative response spectrum was recorded at room temperature using a Fourier transform infrared spectrometer (Nicolet, 8700). The transient photocurrent response was measured using an oscilloscope (Tektronix, DPO 5204) at 2 μm to analyze the photoresponse time. All measurements were conducted at room temperature. The blackbody tests were performed using a calibrated commercial blackbody furnace (HFY-206A). After modulation by a chopper, the photocurrent signal was transformed into a voltage signal using a current preamplifier (Stanford Research Systems,

SR570) and recorded by a lock-in amplifier (Ametek, 7270 DSP) in real time. The noise spectrum was measured using an N9010B signal analyzer (Keysight Technologies, EXA Signal Analyzer) and the SR570 current preamplifier. An eight-channel synchronous 24-bit data acquisition card (VK702H-Pro) was used to read data from the 8 pixels of the photodetector linear array. Open-source image processing library OpenCV was used to perform nonuniformity correction and similarity comparison operations on the images in a Windows environment (Python version 3.10.11, OpenCV version 4.7.0).

Supplementary Materials

This PDF file includes:

Supplementary notes S1 to S8
Table S1
Figs. S1 to S13
References

REFERENCES AND NOTES

1. F. Xia, H. Wang, D. Xiao, M. Dubey, A. Ramasubramaniam, Two-dimensional material nanophotonics. *Nat. Photonics* **8**, 899–907 (2014).
2. F. H. L. Koppens, T. Mueller, P. Avouris, A. C. Ferrari, M. S. Vitiello, M. Polini, Photodetectors based on graphene, other two-dimensional materials and hybrid systems. *Nat. Nanotechnol.* **9**, 780–793 (2014).
3. N. Huo, G. Konstantatos, Recent progress and future prospects of 2D-based photodetectors. *Adv. Mater.* **30**, e1801164 (2018).
4. A. Soibel, D. Z. Ting, C. J. Hill, A. M. Fisher, L. Hoglund, S. A. Keo, S. D. Gunapala, Mid-wavelength infrared InAsSb/InSb nBn detector with extended cut-off wavelength. *Appl. Phys. Lett.* **109**, 103505 (2016).
5. Y. Wang, Y. Gu, A. Cui, Q. Li, T. He, K. Zhang, Z. Wang, Z. Li, Z. Zhang, P. Wu, R. Xie, F. Wang, P. Wang, C. Shan, H. Li, Z. Ye, P. Zhou, W. Hu, Fast uncooled mid-wavelength infrared photodetectors with heterostructures of van der Waals on epitaxial HgCdTe. *Adv. Mater.* **34**, e2107772 (2022).
6. D. Alshahrani, M. Kesaria, J. J. Jiménez, D. Kwan, V. Srivastava, M. Delmas, F. M. Morales, B. Liang, D. Huffaker, Effect of interfacial schemes on the optical and structural properties of InAs/GaSb type-II superlattices. *ACS Appl. Mater. Interfaces* **15**, 8624–8635 (2023).
7. A. Rogalski, Progress in focal plane array technologies. *Prog. Quantum Electron.* **36**, 342–473 (2012).
8. Y. Xie, B. Zhang, S. Wang, D. Wang, A. Wang, Z. Wang, H. Yu, H. Zhang, Y. Chen, M. Zhao, B. Huang, L. Mei, J. Wang, Ultrabroadband MoS_2 photodetector with spectral response from 445 to 2717 nm. *Adv. Mater.* **29**, 1605972 (2017).
9. W. Li, L. Liu, Q. Tao, Y. Chen, Z. Lu, L. Kong, W. Dang, W. Zhang, Z. Li, Q. Li, J. Tang, L. Ren, W. Song, X. Duan, C. Ma, Y. Xiang, L. Liao, Y. Liu, Realization of ultra-scaled MoS_2 vertical diodes via double-side electrodes lamination. *Nano Lett.* **22**, 4429–4436 (2022).
10. N. Huo, G. Konstantatos, Ultrasensitive all-2D MoS_2 phototransistors enabled by an out-of-plane MoS_2 PN homojunction. *Nat. Commun.* **8**, 572 (2017).
11. F. Zhong, J. Ye, T. He, L. Zhang, Z. Wang, Q. Li, B. Han, P. Wang, P. Wu, Y. Yu, J. Guo, Z. Zhang, M. Peng, T. Xu, X. Ge, Y. Wang, H. Wang, M. Zubair, X. Zhou, P. Gao, Z. Fan, W. Hu, Substitutionally doped $MoSe_2$ for high-performance electronics and optoelectronics. *Small* **17**, e2102855 (2021).
12. A. Varghese, D. Saha, K. Thakar, V. Jindal, S. Ghosh, N. V. Medhekar, S. Ghosh, S. Lodha, Near-direct bandgap WSe_2/ReS_2 type-II pn heterojunction for enhanced ultrafast photodetection and high-performance photovoltaics. *Nano Lett.* **20**, 1707–1717 (2020).
13. D. Jariwala, V. K. Sangwan, C.-C. Wu, P. L. Prabhumirashi, M. L. Geier, T. J. Marks, L. J. Lauhon, M. C. Hersam, Gate-tunable carbon nanotube–MoS_2 heterojunction p-n diode. *Proc. Natl. Acad. Sci. U.S.A.* **110**, 18076–18080 (2013).
14. Y. Wen, L. Yin, P. He, Z. Wang, X. Zhang, Q. Wang, T. A. Shifa, K. Xu, F. Wang, X. Zhan, F. Wang, C. Jiang, J. He, Integrated high-performance infrared phototransistor arrays composed of nonlayered PbS–MoS_2 heterostructures with edge contacts. *Nano Lett.* **16**, 6437–6444 (2016).
15. S. Hong, N. Zagni, S. Choo, N. Liu, S. Baek, A. Bala, H. Yoo, B. H. Kang, H. J. Kim, H. J. Yun, M. A. Alam, S. Kim, Highly sensitive active pixel image sensor array driven by large-area bilayer MoS_2 transistor circuitry. *Nat. Commun.* **12**, 3559 (2021).
16. B. Sun, L. Kong, G. Li, Q. Su, X. Zhang, Z. Liu, Y. Peng, G. Liao, T. Shi, Fully integrated photodetector array based on an electrochemically exfoliated, atomically thin MoS_2 film for photoimaging. *ACS Appl. Electron. Mater.* **4**, 1010–1018 (2022).
17. Q. Zhu, Y. Chen, X. Zhu, Y. Sun, Z. Cheng, J. Xu, M. Xu, High-performance near-infrared $PtSe_2$/n-Ge heterojunction photodetector with ultrathin Al_2O_3 passivation interlayer. *Sci. China Mater.* **66**, 2777–2787 (2023).
18. L. Zeng, D. Wu, J. Jie, X. Ren, X. Hu, S. P. Lau, Y. Chai, Y. H. Tsang, Van der Waals epitaxial growth of mosaic-like 2D platinum ditelluride layers for room-temperature mid-infrared photodetection up to 10.6 μm. *Adv. Mater.* **32**, e2004412 (2020).
19. L. Li, Y. Yu, G. J. Ye, Q. Ge, X. Ou, H. Wu, D. Feng, X. H. Chen, Y. Zhang, Black phosphorus field-effect transistors. *Nat. Nanotechnol.* **9**, 372–377 (2014).
20. M. Amani, E. Regan, J. Bullock, G. H. Ahn, A. Javey, Mid-wave infrared photoconductors based on black phosphorus-arsenic alloys. *ACS Nano* **11**, 11724–11731 (2017).
21. H. Yuan, X. Liu, F. Afshinmanesh, W. Li, G. Xu, J. Sun, B. Lian, A. G. Curto, G. Ye, Y. Hikita, Z. Shen, S.-C. Zhang, X. Chen, M. Brongersma, H. Y. Hwang, Y. Cui, Polarization-sensitive broadband photodetector using a black phosphorus vertical p–n junction. *Nat. Nanotechnol.* **10**, 707–713 (2015).
22. J. Bullock, M. Amani, J. Cho, Y.-Z. Chen, G. H. Ahn, V. Adinolfi, V. R. Shrestha, Y. Gao, K. B. Crozier, Y.-L. Chueh, A. Javey, Polarization-resolved black phosphorus/molybdenum disulfide mid-wave infrared photodiodes with high detectivity at room temperature. *Nat. Photonics* **12**, 601–607 (2018).
23. L. Ye, P. Wang, W. Luo, F. Gong, L. Liao, T. Liu, L. Tong, J. Zang, J. Xu, W. Hu, Highly polarization sensitive infrared photodetector based on black phosphorus-on-WSe_2 photogate vertical heterostructure. *Nano Energy* **37**, 53–60 (2017).
24. S. Lee, R. Peng, C. Wu, M. Li, Programmable black phosphorus image sensor for broadband optoelectronic edge computing. *Nat. Commun.* **13**, 1485 (2022).
25. H. Kim, S. Z. Uddin, D.-H. Lien, M. Yeh, N. S. Azar, S. Balendhran, T. Kim, N. Gupta, Y. Rho, C. P. Grigoropoulos, K. B. Crozier, A. Javey, Actively variable-spectrum optoelectronics with black phosphorus. *Nature* **596**, 232–237 (2021).
26. S. Yuan, D. Naveh, K. Watanabe, T. Taniguchi, F. Xia, A wavelength-scale black phosphorus spectrometer. *Nat. Photonics* **15**, 601–607 (2021).
27. Y. Chen, Y. Wang, Z. Wang, Y. Gu, Y. Ye, X. Chai, J. Ye, Y. Chen, R. Xie, Y. Zhou, Z. Hu, Q. Li, L. Zhang, F. Wang, P. Wang, J. Miao, J. Wang, X. Chen, W. Lu, P. Zhou, W. Hu, Unipolar barrier photodetectors based on van der Waals heterostructures. *Nat. Electron.* **4**, 357–363 (2021).
28. P. Wu, L. Ye, L. Tong, P. Wang, Y. Wang, H. Wang, H. Ge, Z. Wang, Y. Gu, K. Zhang, Y. Yu, M. Peng, F. Wang, M. Huang, P. Zhou, W. Hu, Van der Waals two-color infrared photodetector. *Light Sci. Appl.* **11**, 6 (2022).
29. L. Ye, H. Li, Z. Chen, J. Xu, Near-infrared photodetector based on MoS_2/black phosphorus heterojunction. *ACS Photonics* **3**, 692–699 (2016).
30. C. R. Dean, A. F. Young, I. Meric, C. Lee, L. Wang, S. Sorgenfrei, K. Watanabe, T. Taniguchi, P. Kim, K. L. Shepard, J. Hone, Boron nitride substrates for high-quality graphene electronics. *Nat. Nanotechnol.* **5**, 722–726 (2010).
31. H. Jawa, A. Varghese, S. Ghosh, S. Sahoo, Y. Yin, N. V. Medhekar, S. Lodha, Wavelength-controlled photocurrent polarity switching in BP-MoS_2 heterostructure. *Adv. Funct. Mater.* **32**, 2112696 (2022).
32. X. Chen, X. Lu, B. Deng, O. Sinai, Y. Shao, C. Li, S. Yuan, V. Tran, K. Watanabe, T. Taniguchi, D. Naveh, L. Yang, F. Xia, Widely tunable black phosphorus mid-infrared photodetector. *Nat. Commun.* **8**, 1672 (2017).
33. L. Tao, H. Li, Y. Gao, Z. Chen, L. Wang, Y. Deng, J. Zhang, J. Xu, Deterministic and etching-free transfer of large-scale 2D layered materials for constructing interlayer coupled van der Waals heterostructures. *Adv. Mater. Technol.* **3**, 1700282 (2018).
34. D. G. Purdie, N. M. Pugno, T. Taniguchi, K. Watanabe, A. C. Ferrari, A. Lombardo, Cleaning interfaces in layered materials heterostructures. *Nat. Commun.* **9**, 5387 (2018).
35. K. Kinoshita, R. Moriya, M. Onodera, Y. Wakafuji, S. Masubuchi, K. Watanabe, T. Taniguchi, T. Machida, Dry release transfer of graphene and few-layer h-BN by utilizing thermoplasticity of polypropylene carbonate. *NPJ 2D Mater. Appl.* **3**, 22 (2019).
36. T. Iwasaki, K. Endo, E. Watanabe, D. Tsuya, Y. Morita, S. Nakaharai, Y. Noguchi, Y. Wakayama, K. Watanabe, T. Taniguchi, S. Moriyama, Bubble-free transfer technique for high-quality graphene/hexagonal boron nitride van der Waals heterostructures. *ACS Appl. Mater. Interfaces* **12**, 8533–8538 (2020).
37. J. Chen, L. Liu, H. Chen, N. Xu, S. Deng, Controlled preparation of high quality bubble-free and uniform conducting interfaces of vertical van der Waals heterostructures of arrays. *ACS Appl. Mater. Interfaces* **16**, 10877–10885 (2024).
38. F. Wang, T. Zhang, R. Xie, Z. Wang, W. Hu, How to characterize figures of merit of two-dimensional photodetectors. *Nat. Commun.* **14**, 2224 (2023).
39. G.-X. Ni, Y. Zheng, S. Bae, H. R. Kim, A. Pachoud, Y. S. Kim, C.-L. Tan, D. Im, J.-H. Ahn, B. H. Hong, B. Özyilmaz, Quasi-periodic nanoripples in graphene grown by chemical vapor deposition and its impact on charge transport. *ACS Nano* **6**, 1158–1164 (2012).
40. H. Fang, W. Hu, Photogating in low dimensional photodetectors. *Adv. Sci.* **4**, 1700323 (2017).
41. Y. Liu, S. Liu, Z. Wang, B. Li, K. Watanabe, T. Taniguchi, W. J. Yoo, J. Hone, Low-resistance metal contacts to encapsulated semiconductor monolayers with long transfer length. *Nat. Electron.* **5**, 579–585 (2022).
42. T. Uwanno, Y. Hattori, T. Taniguchi, K. Watanabe, K. Nagashio, Fully dry PMMA transfer of graphene on *h*-BN using a heating/cooling system. *2D Mater.* **2**, 041002 (2015).
43. A. Rogalski, Scaling infrared detectors—Status and outlook. *Rep. Prog. Phys.* **85**, 126501 (2022).

44. R. Dagan, Y. Vaknin, A. Henning, J. Y. Shang, L. J. Lauhon, Y. Rosenwaks, Two-dimensional charge carrier distribution in MoS_2 monolayer and multilayers. *Appl. Phys. Lett.* **114**, 101602 (2019).
45. T. Li, W. Guo, L. Ma, W. Li, Z. Yu, Z. Han, S. Gao, L. Liu, D. Fan, Z. Wang, Y. Yang, W. Lin, Z. Luo, X. Chen, N. Dai, X. Tu, D. Pan, Y. Yao, P. Wang, Y. Nie, J. Wang, Y. Shi, X. Wang, Epitaxial growth of wafer-scale molybdenum disulfide semiconductor single crystals on sapphire. *Nat. Nanotechnol.* **16**, 1201–1207 (2021).
46. Y. Liu, X. Duan, H.-J. Shin, S. Park, Y. Huang, X. Duan, Promises and prospects of two-dimensional transistors. *Nature* **591**, 43–53 (2021).
47. P. Wang, S. Liu, W. Luo, H. Fang, F. Gong, N. Guo, Z.-G. Chen, J. Zou, Y. Huang, X. Zhou, J. Wang, X. Chen, W. Lu, F. Xiu, W. Hu, Arrayed van der Waals broadband detectors for dual-band detection. *Adv. Mater.* **29**, 1604439 (2017).
48. Y. Jeon, J. Seo, J. Kim, D. Rhee, M. Jung, H. Park, J. Kang, Wafer-scale two-dimensional molybdenum diselenide phototransistor array via liquid-precursor-assisted chemical vapor deposition. *Adv. Opt. Mater.* **10**, 2101492 (2022).
49. A. Bala, M. Sritharan, N. Liu, M. Naqi, A. Sen, G. Han, H. Y. Rho, Y. Yoon, S. Kim, Active pixel image sensor array for dual vision using large-area bilayer WS_2. *InfoMat* **6**, e12513 (2024).
50. K. Y. Thai, I. Park, B. J. Kim, A. T. Hoang, Y. Na, C. U. Park, Y. Chae, J.-H. Ahn, MoS_2/graphene photodetector array with strain-modulated photoresponse up to the near-infrared regime. *ACS Nano* **15**, 12836–12846 (2021).
51. D. Geum, S. Kim, J. Khym, J. Lim, S. Kim, S. Ahn, T. S. Kim, K. Kang, S. Kim, Arrayed MoS_2-$In_{0.53}Ga_{0.47}As$ van der Waals heterostructure for high-speed and broadband detection from visible to shortwave-infrared light. *Small* **17**, e2007357 (2021).
52. R. K. Saroj, P. Guha, S. Lee, D. Yoo, E. Lee, J. Lee, M. Kim, G. Yi, Photodetector arrays based on MBE-grown GaSe/graphene heterostructure. *Adv. Opt. Mater.* **10**, 2200332 (2022).
53. Y. Lu, Y. Wang, C. Xu, C. Xie, W. Li, J. Ding, W. Zhou, Z. Qin, X. Shen, L.-B. Luo, Construction of $PtSe_2$/Ge heterostructure-based short-wavelength infrared photodetector array for image sensing and optical communication applications. *Nanoscale* **13**, 7606–7612 (2021).
54. P. Li, H. Wang, M. Yu, Y. Li, Overview of image smoothing algorithms. *J. Phys. Conf. Ser.* **1883**, 012024 (2021).
55. S. Nakariyakul, Fast spatial averaging: An efficient algorithm for 2D mean filtering. *J. Supercomput.* **65**, 262–273 (2013).
56. A. Makandar, B. Halalli, Image enhancement techniques using highpass and lowpass filters. *Int. J. Comput. Appl.* **109**, 21–27 (2015).
57. X. Liu, X. Lu, H. Shen, Q. Yuan, Y. Jiao, L. Zhang, Stripe noise separation and removal in remote sensing images by consideration of the global sparsity and local variational properties. *IEEE Trans. Geosci. Remote Sens.* **54**, 3049–3060 (2016).
58. P. Jagalingam, A. V. Hegde, A review of quality metrics for fused image. *Aquat. Procedia* **4**, 133–142 (2015).
59. U. Sara, M. Akter, M. S. Uddin, Image quality assessment through FSIM, SSIM, MSE and PSNR—A comparative study. *J. Comput. Commun.* **07**, 8–18 (2019).
60. Z. Wu, Y. Lyu, Y. Zhang, R. Ding, B. Zheng, Z. Yang, S. P. Lau, X. H. Chen, J. Hao, Large-scale growth of few-layer two-dimensional black phosphorus. *Nat. Mater.* **20**, 1203–1209 (2021).
61. C. Chen, Y. Yin, R. Zhang, Q. Yuan, Y. Xu, Y. Zhang, J. Chen, Y. Zhang, C. Li, J. Wang, J. Li, L. Fei, Q. Yu, Z. Zhou, H. Zhang, R. Cheng, Z. Dong, X. Xu, A. Pan, K. Zhang, J. He, Growth of single-crystal black phosphorus and its alloy films through sustained feedstock release. *Nat. Mater.* **22**, 717–724 (2023).
62. Z. Shi, X. Ren, H. Qiao, R. Cao, Y. Zhang, X. Qi, H. Zhang, Recent insights into the robustness of two-dimensional black phosphorous in optoelectronic applications. *J. Photochem. Photobiol. C Photochem. Rev.* **43**, 100354 (2020).
63. M. Peng, R. Xie, Z. Wang, P. Wang, F. Wang, H. Ge, Y. Wang, F. Zhong, P. Wu, J. Ye, Q. Li, L. Zhang, X. Ge, Y. Ye, Y. Lei, W. Jiang, Z. Hu, F. Wu, X. Zhou, J. Miao, J. Wang, H. Yan, C. Shan, J. Dai, C. Chen, X. Chen, W. Lu, W. Hu, Blackbody-sensitive room-temperature infrared photodetectors based on low-dimensional tellurium grown by chemical vapor deposition. *Sci. Adv.* **7**, eabf7358 (2021).
64. L. Tong, X. Huang, P. Wang, L. Ye, M. Peng, L. An, Q. Sun, Y. Zhang, G. Yang, Z. Li, F. Zhong, F. Wang, Y. Wang, M. Motlag, W. Wu, G. J. Cheng, W. Hu, Stable mid-infrared polarization imaging based on quasi-2D tellurium at room temperature. *Nat. Commun.* **11**, 2308 (2020).
65. G. Kresse, J. Furthmüller, Efficient iterative schemes for ab initio total-energy calculations using a plane-wave basis set. *Phys. Rev. B* **54**, 11169–11186 (1996).
66. G. Kresse, J. Furthmüller, Efficiency of ab-initio total energy calculations for metals and semiconductors using a plane-wave basis set. *Comput. Mater. Sci.* **6**, 15–50 (1996).
67. P. E. Blöchl, Projector augmented-wave method. *Phys. Rev. B* **50**, 17953–17979 (1994).
68. J. P. Perdew, K. Burke, M. Ernzerhof, Generalized gradient approximation made simple. *Phys. Rev. Lett.* **77**, 3865–3868 (1996).
69. S. Grimme, J. Antony, S. Ehrlich, H. Krieg, A consistent and accurate *ab initio* parametrization of density functional dispersion correction (DFT-D) for the 94 elements H-Pu. *J. Chem. Phys.* **132**, 154104 (2010).
70. T. Wang, R. Wang, P. Yuan, S. Xu, J. Liu, X. Wang, Interfacial thermal conductance between mechanically exfoliated black phosphorus and SiO_x : Effect of thickness and temperature. *Adv. Mater. Interfaces* **4**, 1700233 (2017).
71. P. K. Saxena, Numerical study of dual band (MW/LW) IR detector for performance improvement. *Def. Sci. J.* **67**, 141–148 (2017).
72. A. Rogalski, *Infrared Detectors* (Taylor & Francis, ed.2, 2011).
73. F. Wu, Q. Li, P. Wang, H. Xia, Z. Wang, Y. Wang, M. Luo, L. Chen, F. Chen, J. Miao, X. Chen, W. Lu, C. Shan, A. Pan, X. Wu, W. Ren, D. Jariwala, W. Hu, High efficiency and fast van der Waals hetero-photodiodes with a unilateral depletion region. *Nat. Commun.* **10**, 4663 (2019).
74. D. Wu, R. Tian, P. Lin, Z. Shi, X. Chen, M. Jia, Y. Tian, X. Li, L. Zeng, J. Jie, Wafer-scale synthesis of wide bandgap 2D $GeSe_2$ layers for self-powered ultrasensitive UV photodetection and imaging. *Nano Energy* **104**, 107972 (2022).
75. X.-W. Tong, Y.-N. Lin, R. Huang, Z.-X. Zhang, C. Fu, D. Wu, L.-B. Luo, Z.-J. Li, F.-X. Liang, W. Zhang, Direct tellurization of Pt to synthesize 2D $PtTe_2$ for high-performance broadband photodetectors and NIR image sensors. *ACS Appl. Mater. Interfaces* **12**, 53921–53931 (2020).
76. S. J. R. Tan, I. Abdelwahab, L. Chu, S. M. Poh, Y. Liu, J. Lu, W. Chen, K. P. Loh, Quasi-monolayer black phosphorus with high mobility and air stability. *Adv. Mater.* **30**, 1704619 (2018).
77. G. Long, D. Maryenko, J. Shen, S. Xu, J. Hou, Z. Wu, W. K. Wong, T. Han, J. Lin, Y. Cai, R. Lortz, N. Wang, Achieving ultrahigh carrier mobility in two-dimensional hole gas of black phosphorus. *Nano Lett.* **16**, 7768–7773 (2016).
78. Y. Zhao, H. Wang, H. Huang, Q. Xiao, Y. Xu, Z. Guo, H. Xie, J. Shao, Z. Sun, W. Han, X. Yu, P. Li, P. K. Chu, Surface coordination of black phosphorus for robust air and water stability. *Angew. Chem. Int. Ed.* **55**, 5003–5007 (2016).
79. J. D. Wood, S. A. Wells, D. Jariwala, K.-S. Chen, E. Cho, V. K. Sangwan, X. Liu, L. J. Lauhon, T. J. Marks, M. C. Hersam, Effective passivation of exfoliated black phosphorus transistors against ambient degradation. *Nano Lett.* **14**, 6964–6970 (2014).
80. G. Qiu, C. Niu, Y. Wang, M. Si, Z. Zhang, W. Wu, P. D. Ye, Quantum hall effect of Weyl fermions in n-type semiconducting tellurene. *Nat. Nanotechnol.* **15**, 585–591 (2020).
81. L. Liu, T. Li, L. Ma, W. Li, S. Gao, W. Sun, R. Dong, X. Zou, D. Fan, L. Shao, C. Gu, N. Dai, Z. Yu, X. Chen, X. Tu, Y. Nie, P. Wang, J. Wang, Y. Shi, X. Wang, Uniform nucleation and epitaxy of bilayer molybdenum disulfide on sapphire. *Nature* **605**, 69–75 (2022).
82. X. Xu, Y. Pan, S. Liu, B. Han, P. Gu, S. Li, W. Xu, Y. Peng, Z. Han, J. Chen, P. Gao, Y. Ye, Seeded 2D epitaxy of large-area single-crystal films of the van der Waals semiconductor 2H $MoTe_2$. *Science* **372**, 195–200 (2021).
83. M. Peng, Y. Yu, Z. Wang, X. Fu, Y. Gu, Y. Wang, K. Zhang, Z. Zhang, M. Huang, Z. Cui, F. Zhong, P. Wu, J. Ye, T. Xu, Q. Li, P. Wang, F. Yue, F. Wu, J. Dai, C. Chen, W. Hu, Room-temperature blackbody-sensitive and fast infrared photodetectors based on 2D tellurium/graphene Van der Waals heterojunction. *ACS Photonics* **9**, 1775–1782 (2022).
84. Y. Wu, S.-E. Wu, J. Hei, L. Zeng, P. Lin, Z. Shi, Q. Chen, X. Li, X. Yu, D. Wu, Van der Waals integration inch-scale 2D $MoSe_2$ layers on Si for highly-sensitive broadband photodetection and imaging. *Nano Res.* **16**, 11422–11429 (2023).
85. Y. Liu, H. Hu, M. Yuan, H. Yin, Y. Qu, Y. Tan, F. Chen, Red-sensitive image array based on defect-engineered PBDB-T/$WSe_{1.5}$-WSe_2/graphene heterostructure. *Adv. Electron. Mater.* **9**, 2300115 (2023).
86. Y. Gong, P. Xie, X. Xing, Z. Lv, T. Xie, S. Zhu, H. Hsu, Y. Zhou, S. Han, Bioinspired artificial visual system based on 2D WSe_2 synapse array. *Adv. Funct. Mater.* **33**, 2303539 (2023).
87. Y.-C. Chen, Y.-J. Lu, Q. Liu, C.-N. Lin, J. Guo, J.-H. Zang, Y.-Z. Tian, C.-X. Shan, Ga_2O_3 photodetector arrays for solar-blind imaging. *J. Mater. Chem. C* **7**, 2557–2562 (2019).
88. T. Wang, D. Zheng, K. Vegso, N. Mrkyvkova, P. Siffalovic, T. Pauporté, High-resolution and stable ruddlesden–popper quasi-2D perovskite flexible photodetectors arrays for potential applications as optical image sensor. *Adv. Funct. Mater.* **33**, 2304659 (2023).
89. H. Wang, L. Li, J. Ma, J. Li, D. Li, 2D perovskite narrowband photodetector arrays. *J. Mater. Chem. C* **9**, 11085–11090 (2021).
90. Z. Zhang, C. Xu, C. Zhu, X. Tong, C. Fu, J. Wang, Y. Cheng, L. Luo, Fabrication of $MAPbI_3$ perovskite/Si heterojunction photodetector arrays for image sensing application. *Sens. Actuators Phys.* **332**, 113176 (2021).

Acknowledgments

Funding: This work is supported by the National Key Research and Development Program of China (grant no. 2023YFB3611400), Strategic Priority Research Program (B) of the Chinese Academy of Sciences (XDB0580000), National Natural Science Foundation of China (grant nos. 62122081, 62305079, 62327812, and 62361136587), Youth Innovation Promotion Association CAS, and Science and Technology Commission of Shanghai Municipality (grant no. 21JC1406100). **Author contributions:** W.H. and P.W. proposed the research methodology and experimental design. Z.W. and Q.L. provided supervision and guidance throughout the study. T.X. and F.Z. were responsible for the majority of the experiments and obtained the experimental data. F.Z. designed the passive imaging

system. X.G. was responsible for the theoretical DFT calculations. J.W. provided crucial assistance for nonuniformity correction of the images. H.W. and R.J. assisted with device performance testing. K.Z. tested the noise current spectrum of the devices. Z.Z. conducted the reactive ion etching. T.Z. and Y.Y. performed the AFM measurements. M.L., Y.W., F.W., and F.C. contributed critical insights and expertise to improve the content. All authors participated in the discussion of the results, reviewed, and revised the manuscript.
Competing interests: The authors declare that they have no competing interests.

Data and materials availability: All data needed to evaluate the conclusions in the paper are present in the paper and/or the Supplementary Materials.

Submitted 22 November 2023
Accepted 27 June 2024
Published 2 August 2024
10.1126/sciadv.adn0560